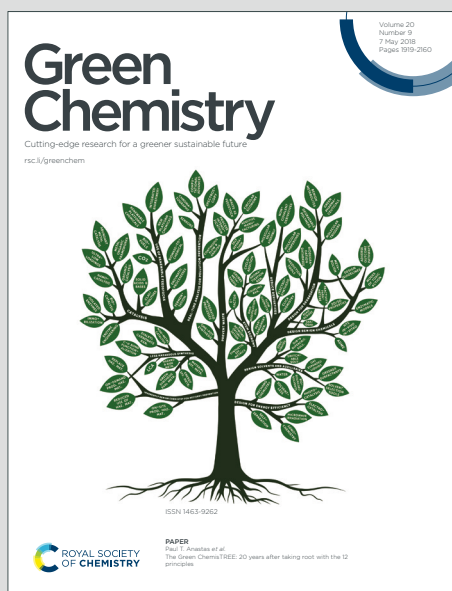


Green Chemistry

Cutting-edge research for a greener sustainable future

Accepted Manuscript

This article can be cited before page numbers have been issued, to do this please use: K. Park, G. H. Gunasekar, S. Kim, H. Park, S. Kim, K. Park, K. Jung and S. Yoon, *Green Chem.*, 2020, DOI: 10.1039/C9GC03685G.



This is an Accepted Manuscript, which has been through the Royal Society of Chemistry peer review process and has been accepted for publication.

Accepted Manuscripts are published online shortly after acceptance, before technical editing, formatting and proof reading. Using this free service, authors can make their results available to the community, in citable form, before we publish the edited article. We will replace this Accepted Manuscript with the edited and formatted Advance Article as soon as it is available.

You can find more information about Accepted Manuscripts in the [Information for Authors](#).

Please note that technical editing may introduce minor changes to the text and/or graphics, which may alter content. The journal's standard [Terms & Conditions](#) and the [Ethical guidelines](#) still apply. In no event shall the Royal Society of Chemistry be held responsible for any errors or omissions in this Accepted Manuscript or any consequences arising from the use of any information it contains.

ARTICLE

CO₂ hydrogenation to formic acid over heterogenized ruthenium catalysts using a fixed bed reactor with separation unitsKwangho Park,^{†a} Gunniya Hariyanandam Gunasekar,^{†b} Seong-Hoon Kim,^c Hongjin Park,^c Samhwan Kim,^d Kiyong Park,^d Kwang-Deog Jung,^{*,b} and Sungho Yoon^{*,c}Received 00th January 20xx,
Accepted 00th January 20xx

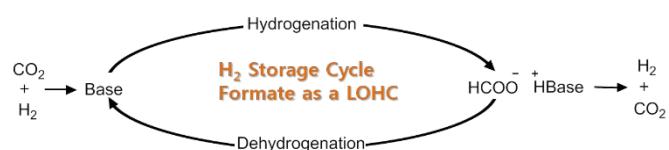
DOI: 10.1039/x0xx00000x

Along with the mitigation of CO₂ emission, recently, the CO₂-derived formic acid process has drawn attention as a promising platform for the renewable-energy-derived hydrogen storage cycle by using formic acid as a liquid organic hydrogen carrier (LOHC). Here, a heterogenized Ru molecular catalyst on a bpyTN-30-CTF support is prepared and successfully implemented in an integrated trickle-bed reactor system for continuous CO₂ hydrogenation to produce formic acid. The bpyTN-30-CTF support with the alternative structure of bpy and TN motif enhances the porosity and metal anchoring sites. The Ru/bpyTN-30-CTF catalyst prepared using the bpyTN-30-CTF support displays sufficient catalytic activity for commercialization. Under the continuous process, the catalyst exhibits substantial catalytic performance with the highest productivity of 669.0 g_{form.} g_{cat.}⁻¹ d⁻¹ with CO₂ conversion of 44.8% for a superficial gas velocity of 72 cm s⁻¹. Furthermore, the catalyst shows excellent stability in the continuous hydrogenation process with a trickle-bed reactor over 30 days of operation reaching the total turnover number of 524,000 without any significant deactivation. Based on kinetic data, a new process to produce formic acid by CO₂ hydrogenation has thus been proposed here.

Introduction

Chemical storage of renewable energy in a secondary energy carrier like hydrogen by water splitting has garnered great interest^{1,2}, because hydrogen has a high gravimetric energy density of 33.3 kWh kg⁻¹ and produces only water as a byproduct during combustion. However, its low volumetric energy density of 2.5 W h L⁻¹ poses a hurdle in its use as an energy carrier³. Therefore, liquid organic hydrogen carriers (LOHCs) have been intensively investigated because of their facile handling for transportation and the scope of hydrogen release by dehydrogenation depending on the purpose^{4,5}. Utilization of CO₂ as a platform molecule to produce LOHCs has been considered a promising strategy for efficient hydrogen storage systems and an alternative method for CO₂ storage at the same time^{6–11}. Particularly, CO₂-derived formic acid is a relevant candidate for hydrogen storage because it can provide 4.4 wt% of hydrogen with perfect atom efficiency

and low toxicity. In addition, the milder energy requisition for the conversion than that of other CO₂-based LOHCs renders formic acid highly attractive for large-scale processes^{12,13}. However, industrial implementation of the formic acid hydrogen storage cycle through hydrogenation and dehydrogenation remains sluggish due to the hurdles suffered by the efficiency. Therefore, the reversible hydrogen charge and discharge processes need to be conducted using appropriate catalytic systems to overcome the kinetic and thermodynamic barriers.



Scheme 1. CO₂-based reversible hydrogen storage cycle using formate as a LOHC

For decades, remarkable progress has been made in the development of efficient catalytic systems to close the formic acid-based hydrogen storage cycle^{14–16}. As a state of the art in dehydrogenation, practical application of formic acid as a hydrogen carrier has been boosted by a smart attempt made by Gabor Laurenczy and coworkers in the École Polytechnique Fédérale de Lausanne and GRT groups. They could generate nominal power of 850 W with electrical efficiency of 45% from formic acid using a Ru-based catalyst¹⁷. In addition, Pidko and co-workers have recently devised Ru-catalyzed integrated 25-kW formic acid-to-power systems, and successfully demonstrated that this compact electricity generator could be applied to the scale of a city bus¹⁸. However, in terms of

^a Department of Applied Chemistry, Kookmin University, 77 Jeongneung-ro, Seongbuk-gu, Seoul, Republic of Korea.

^b Clean Energy Research Centre, Korea Institute of Science and Technology, P.O. Box 131, Cheongryang, Seoul, Republic of Korea

^c Department of Chemistry, Chung Ang University, 84 Heukseok-ro, Dongjak-gu, Seoul, Republic of Korea

^d Department of Chemistry, KAIST, 291 Daehak-ro, Yuseong-gu, Daejeon, Republic of Korea.

[†] These authors contributed equally to this work.

Electronic Supplementary Information (ESI) available: [details of any supplementary information available should be included here]. See DOI: 10.1039/x0xx00000x

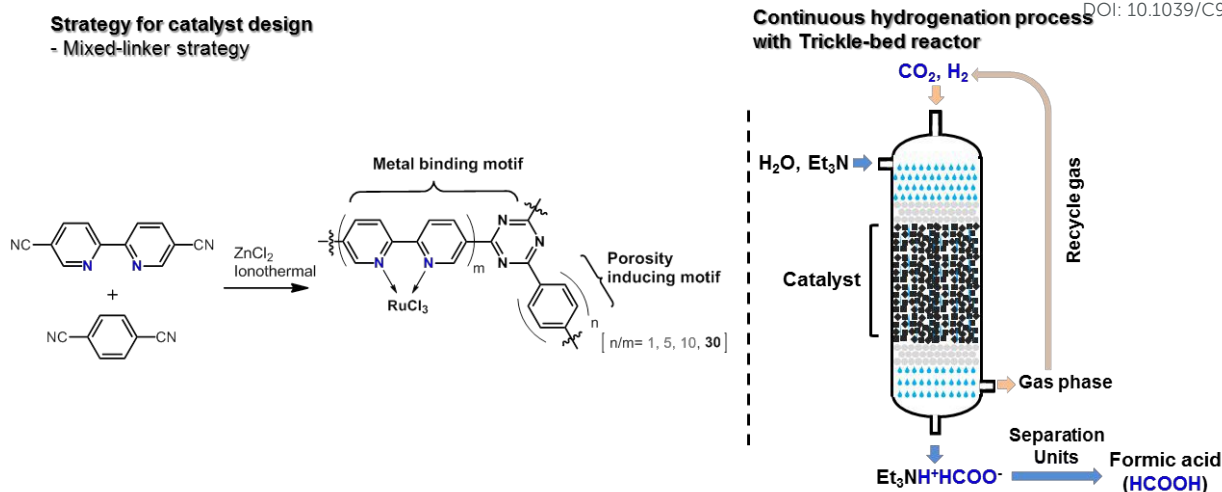


Figure 1 Structural representation of Ru/bpyTN-CTFs synthesis and a schematic of structured CO₂ hydrogenation in trickle-bed reactor

sustainability, formic acid availability from CO₂ hydrogenation on a large scale and its affordable price are crucial prerequisites for the widespread utilization of the technique commercially. Meanwhile, the hydrogenation process significantly lags behind the dehydrogenation owing to the low efficiency. Therefore, the development of a novel system for the production of formic acid by CO₂ hydrogenation has remained challenging for decades in attempts to close the hydrogen cycle and has shown fruitful results.

In the last decades, homogeneous catalytic systems for CO₂ hydrogenation to formic acid have been intensively investigated to demonstrate superior catalytic activity and selectivity^{16,19–24}. Meanwhile, continuous processes with homogeneous systems have been conducted at the laboratory scale and patented by chemical companies^{25–33}. However, homogeneous catalysts should be completely separated from the reaction mixture to be reused; the incomplete recovery of homogeneous catalyst makes formic acid decomposed during the separation process. Toward the realization of formic acid production, heterogeneous systems for catalytic CO₂ hydrogenation are very attractive because they make catalyst separation easy^{21,34–37}. Fachinetti and coworkers have attempted the formation of a total of 1.326 kg of formate using a reactor with supported gold catalyst that could be reused for 37 days without fastidious separation³⁸. Walter Leitner's group has used immobilized catalysis systems with supercritical CO₂ flow for the continuous process of CO₂ hydrogenation, and successfully produced pure formic acid³⁹. However, the slurry reactor requires catalyst separation and the disintegration of catalyst particles results in significant catalyst loss and further commercial implementations is hindered by the low efficiency of heterogeneous systems.

For the preparation of heterogenized catalysts, immobilization of a homogeneous catalyst on catalytic supports via the formation of covalent bonds has garnered much interest in the context of CO₂ hydrogenation to formic acid, as the method combines the advantages of homogeneous and heterogeneous systems^{34–37}. In particular, various advantageous properties

induced by a rationally designed catalyst support such as enhanced porosity and the presence of various heteroatom ligand sites enable diversification of heterogenized catalytic systems. Previously, we reported a Ru molecular catalyst heterogenized on a bipyridine functionalized covalent triazine framework (CTF), which exhibited high efficiency with exceptional stability during successive runs in a batch reactor^{40–42}. The consequent robustness and outstanding catalytic activity of the CTF-based molecular Ru catalyst encouraged us to investigate the continuous production of formate via CO₂ hydrogenation. Very recently, Urakawa's group reported that Ir molecular catalyst heterogenized on CTF was successfully demonstrated to be active under high-pressure condition for continuous CO₂ hydrogenation to formic acid. Further, they elucidated that the rich nitrogen content on the pore surface of CTF support is to assist for the carbon dioxide in close proximity to the active site of the catalyst. However, it is still required to attain high productivity for commercial feasibility⁴³. In this paper, we present a Ru molecular catalyst heterogenized on a bipyridine (bpy)-terephthalonitrile (TN) mixed-CTF (Ru/bpyTN-30-CTF) system for the continuous hydrogenation of CO₂ to formate in a trickle-bed reactor, which is a conventional fixed-bed reactor (Figure 1)⁴⁴. The heterogenized catalyst produced formate at 669.0 g_{form.} g_{cat.}⁻¹ d⁻¹ with a CO₂ conversion of 44.8 % for a superficial gas velocity of 72 cm s⁻¹, also exhibiting excellent stability with the total turnover number of 524,000 for 30 days without deactivation. This may be attributed to the enhanced surface area induced by the TN-based skeletal framework that helps the reactive metal centers to be more efficiently dispersed on the support pore surface, which plays a key role in ensuring improved interaction of reagents with the catalytic active sites, as well as the stable binding environment arising from the bidentate coordination of the RuCl₃-bpy motif.

Experimental

Materials and instrumentation

All chemicals were purchased from commercial suppliers and used without further purifications. 2-bromo-5-cyanopyridine (>99%) and terephthalonitrile (>98%) were purchased from T.C.I. chemicals. Ruthenium(III) chloride hydrate, zinc(II) chloride (ZnCl_2) (>98%), nickel chloride hexahydrate, lithium chloride, triethylamine (Et_3N), zinc dust, iodine, anhydrous methylene chloride, and anhydrous dimethylformamide were purchased from Sigma Aldrich. 5,5'-dicyano-2,2'-bipyridine (DCBPY) was synthesized according to a previous report⁴⁵. CO_2 and N_2 were obtained from Sinyang Gas Industries.

Fourier transform infrared (FT-IR) analysis was performed on a Nicolet iS 10 with MCT detector (Thermo Fisher Scientific) by the KBr pellet technique. Scanning electron microscopy (SEM) and energy dispersive spectrometry (EDS) measurements were performed on a JEOL LTD (JAPAN) JEM-7610F operated at an accelerating voltage of 20.0 kV. N_2 adsorption-desorption measurements were conducted at 77 K using a BELSORP mini II (JAPAN). The samples were degassed for 1 day at 150 °C before the measurements. Powder X-ray diffraction (PXRD) was performed on a RIGAKU D/Max 2500 V using Cu (40 kV, 30 mA) radiation. Elemental analysis (EA) was performed with an elemental analyzer (Vario Micro cube, Germany). Thermogravimetric analysis (TGA) and differential thermal analysis (DTA) were performed on a Q600 analyzer (TA Instrument, US). The experiments were carried out at a heating rate of 10 °C per minute up to 700 °C under a nitrogen atmosphere. The ruthenium content was determined by inductively coupled plasma optical emission spectrometry (ICP-OES) (iCAP-6000, Thermo fisher scientific) using a microwave-assisted acid digestion system (MARS6, CEM/U.S.A.). X-ray photoelectron spectroscopy (XPS) analysis was performed on an ESCA 2000 (VG Microtech) at a pressure of $\sim 3 \times 10^{-9}$ mbar using Al K α as the excitation source ($h\nu = 1486.6$ eV) with a concentric hemispherical analyzer. High-angle annular dark-field imaging transmission electron microscopy (HAADF-TEM) analyses were performed on a Jeol JEM-2100F HRTEM operated at 200 kV. The samples were prepared by dispersing in ethanol and placed on a carbon film grid by dropping and analyzed after drying under vacuum at 60 °C overnight. The concentration of formate was determined by high-performance liquid chromatography (HPLC) on an Aminex HPX-87H column with a RI detector using 5 mM of H_2SO_4 as an eluent. X-ray absorption fine structure (XAFS) measurements were conducted by the 7D beamline of Pohang Light Source (PLS-II, 3.0 GeV, South Korea). The incident X-ray beam was monochromatized using a Si(111) double crystal monochromator. The spectra for K-edges for Ru ($E_0 = 22,117$ eV) were obtained in the fluorescence mode in ambient atmosphere. Gas chromatography was analysed by YL-6500 (Younglin, Rep. of Korea) equipped with a Flame ionization and thermal conductivity detectors, and Mol Sieve 13X and porapak N columns using N_2 as a carrier gas (20 mL/min). Calibrations were determined with a gas mixture containing known amounts (100, 1000, 5000 ppm) of CO and CH_4 . ^{13}C , ^1H NMR spectra were recorded on a Bruker Ascend 400 MHz. Mercury porosimetry was obtained using Mercury porosimeter

(MicroActive Autopore 9600, Micromeritics Inst Inc, USA) in the pressure range of 0.2~61,000 psi. DOI: 10.1039/C9GC03685G

Synthesis of bpyTN-mixed CTFs

DCBPY and TN were mixed in varied molar ratios and ground in a mortar thoroughly to afford homogeneously mixed powders (Table S1). The reagents were transferred to 50 mL glass ampoules and dried under vacuum overnight. Then, ZnCl_2 (5 eq for each ampoule) was charged into the ampoules in a glove box, which were then taken out outside and sealed by a flame. The ampoules were heated in a furnace following the preset temperature program (Table S1). After the reaction, the furnace was cooled to room temperature. The crude product was ground well and stirred with 200 mL of a 1 M HCl aqueous solution for 2 h. The black powder was filtered and washed with 40 mL of water and this process was repeated. The sample was then refluxed with 200 mL of the 1 M HCl aqueous solution overnight. After this, the afforded powder was filtered and washed with a 1 M HCl aqueous solution, water, methanol, acetone (3×200 mL for each solvent). The black solid was dried under vacuum at 150 °C overnight.

Synthesis of Ru/bpyTN-30-CTF

bpyTN-30-CTF (9.38 g) was charged into a solution of RuCl_3 (0.623 g) and anhydrous methanol (300 mL) in a 500 mL round-bottomed flask with a condenser and stirred for 30 min under a nitrogen atmosphere and refluxed for 48 h. After the reaction, the mixture was cooled to room temperature and the black colored powder was filtered (filtrates were kept for ICP-OES measurements) and washed with an excess of methanol (3×500 mL), acetone (3×100 mL), and methylene chloride (3×100 mL). The filtered powder was dried under vacuum at 100 °C overnight.

Hydrogenation procedure in trickle-bed reactor

Continuous hydrogenation was carried out in homemade stainless-steel tubular reactor with an internal diameter of 7 mm and length of 460 mm. In a typical run, the 1.5 g of Ru/bpyTN-30-CTF powder (particle size = 50-200 μm) was charged in the middle of the vertically positioned reactor with the catalyst height of 65 mm and covered by glass wools. To prevent back flow of catalyst, the remaining empty space was filled with 2.5 mm glass beads. After flushing with H_2 and CO_2 , the reactor was pressurized to the desired pressure (60–140 bar) under varied feed gas ($\text{CO}_2:\text{H}_2=1:1$) flows and heated to 60–140 °C before the reaction. The pressure was maintained at the desired temperature using a back-pressure regulator and the H_2 gas flow rate was controlled by the mass flow controller. Liquid CO_2 supply from the siphon cylinder was controlled using a high-pressure liquid pump and gasified by the heating line before addition to the reactor. The distilled water and Et_3N were respectively supplied to the reactor using a high-pressure liquid pump. All the gaseous and liquid feeds were thoroughly homogenized and equilibrated in temperature through the tubular preheating zone (7 mm x 460 mm), which was entirely filled with 2.5 mm glass beads, before

entering into the reactor. The liquid product was collected and analyzed using high-performance liquid chromatography and nuclear magnetic resonance to determine acid to amine ratio (AAR) and the concentration of formate. The gaseous product was collected using gas sampling bag and analyzed by gas chromatography. The production rates of formate, superficial gas and liquid velocities (u_g and u_l), formate productivity, CO_2 conversion, and total turnover number were then calculated using eqn. (1-6):

$$\begin{aligned} \text{Molar production rate of HCOO}^- (\text{mol}_{\text{form.}}/\text{h}) \\ = \text{Et}_3\text{N flow rate} (\text{mol}_{\text{Et}_3\text{N}}/\text{h}) \times \text{AAR} \end{aligned} \quad (1)$$

$$\begin{aligned} \text{Production rate of HCOO}^- (\text{g}_{\text{form.}}/\text{h}) \\ = \text{molar production rate of HCOO}^- (\text{mol}_{\text{form.}}/\text{h}) \times \text{M.W of HCOO}^- \end{aligned} \quad (2)$$

$$\text{Superficial velocity (cm/s)} = \frac{\text{volumetric feed flow rate (ml/s)}}{\text{cross sectional area of the reactor (cm}^2\text{)}} \quad (3)$$

$$\begin{aligned} \text{Formate (HCOO}^-) \text{ productivity} \\ = \frac{\text{production rate of HCOO}^- (\text{g}_{\text{form.}}/\text{h})}{\text{charged catalyst mass (g}_{\text{cat.}})} \times 24 (\text{h/d}) \end{aligned} \quad (4)$$

$$\text{CO}_2 \text{ conversion} = \frac{\text{molar production rate of HCOO}^- (\text{mol}_{\text{form.}}/\text{h})}{\text{CO}_2 \text{ Feed rate (mol}_{\text{CO}_2}/\text{h})} \times 100 \quad (5)$$

$$\begin{aligned} \text{Total turnover number} \\ = \frac{\text{molar production rate of HCOO}^- (\text{mol}_{\text{form.}}/\text{h})}{\text{charged molar content of Ru (mol}_{\text{Ru}})} \times \text{operation time (h)} \end{aligned} \quad (6)$$

Results and Discussion

Synthesis and characterization of heterogeneous Ru/bpyTN-30-CTF catalyst

For an industrially viable catalytic process, several requisites need to be fulfilled by the catalyst, such as long-term stability as well as high performance, and feasibility of affordable large-scale synthesis. In this respect, a CTF-based material is a relevant catalytic support for our purpose as it offers advantages such as high robustness and thermochemical stability⁴⁶. Accordingly, it has been extensively reported that CTF-based heterogenized catalysts show excellent activity and stability in various applications, particularly CO_2 hydrogenation^{40-42, 46-51}. However, given the continuous flow conditions of gas/liquid reagents in the process, the catalyst is required to possess an enhanced surface area for high dispersion of metal centers. Furthermore, additional considerations are required for an economically reasonable synthesis of CTF on a large scale, because the source of the

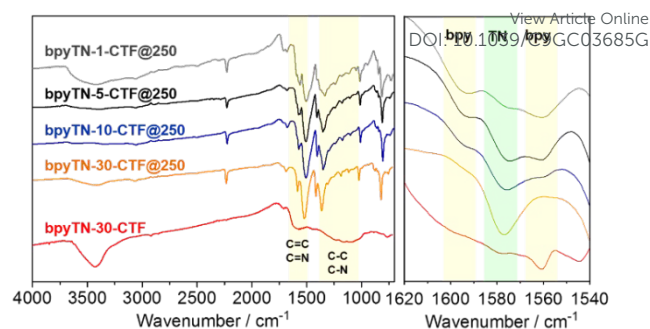


Figure 2. FT-IR spectra of bpy-CTF-250 (gray), bpyTN-1-CTF-250 (black), bpyTN-5-CTF-250 (blue), bpyTN-10-CTF-250 (orange), and bpyTN-30-CTF-250 (red).

CTF support, bpy, is expensive. Accordingly, the mixed-linker strategy was introduced to prepare the function-enhanced and cost-effective CTF support to reduce the catalyst preparation cost through the use of commercially affordable linkers⁵²⁻⁵⁴.

For this purpose, the mixed CTF supports were designed to comprise TN as building blocks for the skeletal structure and bpy as the ligand moiety to stabilize the active metal component. The bpyTN-mixed CTFs were prepared with different ratios of bpy to TN under ionothermal conditions with ZnCl_2 at 250 °C for 72 h to monitor the intact chemical structure preserving from thermal graphitization. FT-IR spectroscopy was used to analyze the functional groups on the architecture of the mixed CTFs (Figure 2). The results revealed vibrations corresponding to the bpy-based motif at 1560 and 1595 cm^{-1} , the TN-based motif at 1580 cm^{-1} , implying C=N and C=C stretching of triazine and pyridine, which indicated the successful formation of a cooperative structure consisting of bpy and TN in the supports. As the ratio of TN to bpy increased, the vibration frequency of TN increased; on the other hand, that of bpy decreased but remained as a shoulder peak, indicating the unchanged presence of bpy. The isotherm revealed that N_2 sorption for bpyTN-mixed CTFs synthesized at 250 °C was almost negligible (Figure S1), which was due to the limited accessibility of the adsorbent into the narrow pores.

To enhance the porosity of the bpyTN-mixed CTFs, the preparation temperature was increased to 400 °C, which is advisable for facile incorporation of metal complexes. Through the N_2 adsorption-desorption isotherm analysis, the porosity of bpyTN-mixed CTFs was confirmed. The adsorption of N_2 in the mixed-CTFs synthesized at 400 °C increased significantly (Figure S2). The sorption followed the typical shape of a type I isotherm, suggesting the presence of abundant micropores. In particular, as the TN ratio compared to bpy increased, the BET surface area of bpyTN-mixed CTF also increased (Table S2), indicating that the TN-based skeletal structure in the framework drove the high surface area on the CTF supports.

Further, elemental analysis was performed to track the outline of the structural change for bpyTN-CTF supports, in comparison to that of bpy-CTF and CTF-1 (Table 1). CTF-1 was prepared using TN only⁴⁶. In the evaluation, C/N ratio of bpy-CTF was found to be 2.59, which was very similar to the calculated value of 2.57. However, as the proportion of TN increased in the support composition, the difference between

Table 1. Elemental analysis of bpyTN-CTFs

Sample	C	N	H	C/N ^a	C/N ^b	Differ. ^c
bpy-CTF	59.72	23.05	3.13	2.59	2.57	0.02
bpyTN-1-CTF	63.88	18.90	3.26	3.38	2.86	0.52
bpyTN-5-CTF	71.71	16.42	2.62	4.37	3.18	1.19
bpyTN-10-CTF	71.14	15.37	2.58	4.63	3.29	1.34
bpyTN-30-CTF	73.12	12.65	2.45	5.78	3.37	2.41
CTF-1	73.79	12.74	2.47	5.79	3.43	2.36

^aExperimentally obtained C/N ratio. ^bTheoretically calculated C/N ratio. ^cDifference between the experimentally obtained and theoretically calculated C/N ratio.

the calculated and experimental C/N ratios gradually increased from 0.52 for bpyTN-1-CTF to 2.41 for, bpyTN-30-CTF indicating the gradually increasing N loss from the support structure. This result implied that the bpy-based structure showed relatively high thermal stability than the TN-based structure and the thermal graphitization phenomenon was predominant with the TN-based structure at high synthetic temperatures. Therefore, it is concluded that the higher degree of thermal graphitization on TN-based structure induced the high surface area to the CTF-based support, which is consistent with the previous result⁵⁵. In the FT-IR measurements, vibrations were observed in the range of 1450–1600 cm⁻¹ (C=N or C=C) and 1000–1400 cm⁻¹ (C-N or C-C), which were broadened due to the thermal graphitization of CTF structure^{55–57}; however, this may still indicate the presence of the bipyridine and triazine site on the CTF support (Figure 2).

We examined the catalytic activity of the prepared four bpyTN-CTFs as preliminary tests under 80 MPa and 120 °C for 2h (CO₂:H₂=1:1) in a batch reactor. The 3 wt% of Ru was metalated to bpyTN-CTFs. Among them, the bpyTN-30-CTF based catalyst showed the highest activity (Table S3), which may be attributed to higher dispersion of Ru cation on the pore surface of bpyTN-30-CTF support than other bpyTN-mixed CTFs. Therefore, bpyTN-30-CTF was chosen as a catalytic support for further studies. The catalyst was also characterized through the nitrogen sorption isotherm analysis, and it was confirmed that the N₂ uptake and BET surface area decreased, when Ru was metalated to bpyTN-30-CTF, i.e., 1010 m² g⁻¹ for the Ru/bpyTN-30-CTF compared to the bpyTN-30-CTF support, i.e., 1251 m² g⁻¹, suggesting the partial occupation of pores by immobilized RuCl₃ units (Table S2 and Figure S3). To examine the thermal stability of the catalyst, TGA was performed. The result revealed that the weight loss of 4.0 % for Ru/bpyTN-30-CTF was observed up to 400 °C except for the 3.3 % weight loss by adsorbed water. This suggested that the catalyst possessed high thermal stability for high reaction temperature in CO₂ hydrogenation. ICP-OES measurements were carried out for both the catalyst and the filtrate to grasp the accurate Ru loading amount. The result showed that the Ru content in the catalyst was 3.03 wt% and was negligible for the filtrate, which indicates almost complete metalation to the support (Table S4).

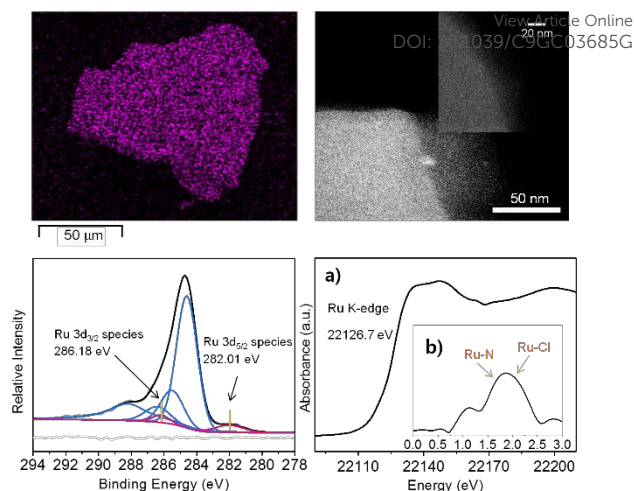


Figure 3. Atomic dispersion of Ru by EDS mapping (top left), HAADF-STEM image (top right), deconvoluted C 1s and Ru 3d XPS spectrum (bottom left), and the normalized XANES spectra at the Ru K-edge (bottom right, a) the k³-weighted EXAFS data in R space for the Ru/bpyTN-30-CTF (bottom right, b)

EDS mapping analyzed the homogeneous distribution of Ru atoms throughout the support, but no distinct Ru particles were found in the HAADF-TEM measurements, suggesting that Ru cations were tightly bounded to the binding sites provided by the support (Figure 3, top left and right, and Figure S5). XPS was measured to determine the more accurate coordination state of Ru atoms on the bpyTN-30-CTF. The observed binding energy of Ru 3d_{5/2} was 282.01 eV, which was fitted to Ru³⁺ oxidation state (Figure 3, bottom left)⁵⁸. It also showed a somewhat reduced binding energy than RuCl₃·xH₂O⁵⁹, which was ascribed to the increased electron density of Ru due to the strong interaction with N-based coordination sites of the support. Ru/bpyTN-30-CTF was also assessed with XAFS analysis (Figure 3, bottom right). Consequently, the normalized shape and edge position in the Ru K-edge X-ray absorption near edge structure (XANES) spectrum were found to be 22126.7 eV, which suggested the presence of Ru in the +3 oxidation state; this result corresponds to the XPS analysis and a previous study. In the extended X-ray absorption fine structure (EXAFS) for Ru/bpyTN-30-CTF, a broad band from 1.5~2.5 Å was observed and this may be assigned to the Ru-Cl peak on ~1.9 Å and to the Ru-N peak on ~1.7 Å, respectively^{60,61}. Therefore, it was concluded that the isolated Ru complex motif was successfully immobilized onto N sites originating from the surface of the bpyTN-30-CTF support.

Catalytic performance tests of Ru/bpyTN-30-CTF with trickle-bed reactor system for continuous CO₂ hydrogenation to formate

Hydrogenation of CO₂ with TBR was driven by a plug-flow type reaction in which gas and liquid reactants were continuously introduced into a fixed-bed catalyst. Because of the short residence time of reactant feed in TBR the diffusion limitation was important for the reaction. Although this type of reactor generally shows a rather lower activity than the stirred batch

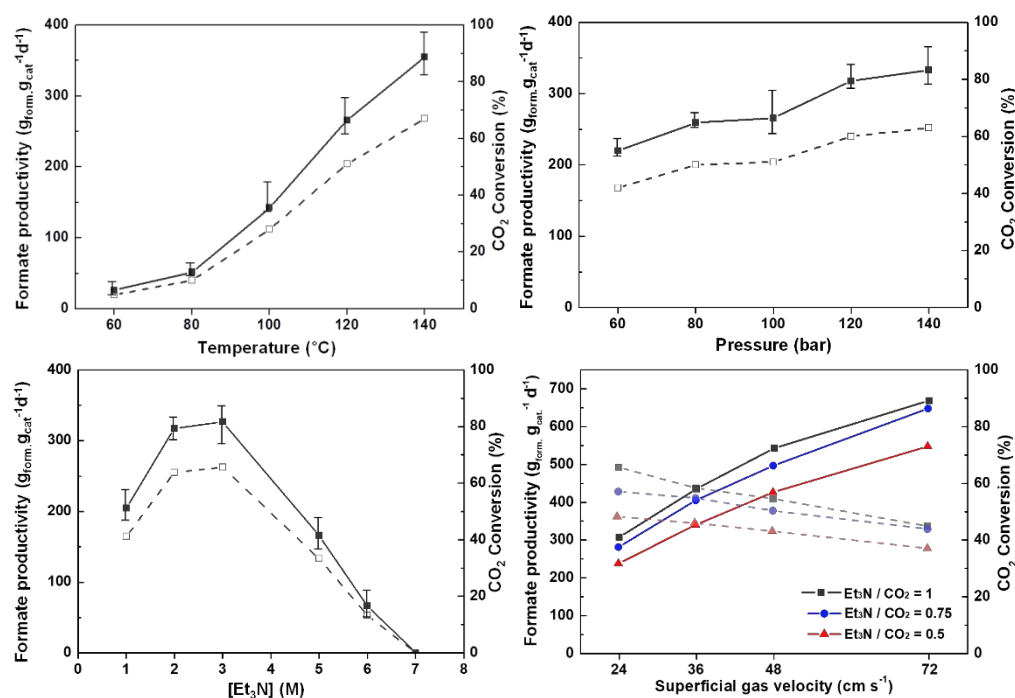


Figure 4. Catalytic CO₂ hydrogenation activities screening in the trickle-bed reactor with the influence of reaction temperature (top left), pressure (top right), concentration of Et₃N (bottom left), and superficial gas velocity (bottom right): (solid line) CO₂ conversion, (dashed line) formate productivity.

reactor, the simple design and operation have advantages over the stirred tank reactor. Additionally, no requirement of the recovery of catalysts during the reaction makes this type of reactor feasible for commercialization.

Under the TBR process, the catalyst selectively converted CO₂ to formate with side products generation only in ppm scale such as CO (300-600 ppm), CH₄ (<5 ppm), and CH₃OH (negligible to detect) (Figure S8-10), representing less than 1% of carbon loss in carbon balance. Therefore, the CO₂ conversion (eqn. 5) was determined based on generated formate amount relative to the input CO₂. The temperature effect on the catalytic activity through the trickle bed was investigated under the conditions of 100 bar and an aqueous 2 M Et₃N solution for a superficial gas velocity of 24 cm s⁻¹ and the temperatures of 60, 80, 100, and 120 °C (Figure 4, top left and Table S9, entry 1-5) in terms of formate productivity and CO₂ conversion. The catalyst showed a formate productivity of 25.9 g_{form} g_{cat}⁻¹ d⁻¹ with 0.05 of acid to amine ratio (AAR) in the product and CO₂ conversion of 5.2% at 60 °C, and both the productivity and CO₂ conversion increased with an increase in the reaction temperature. Here, AAR means a molar ratio of formic acid to Et₃N in reaction products. Finally, the performance of the catalyst showed a productivity of a 355.1 g_{form} g_{cat}⁻¹ d⁻¹ with 0.67 of AAR and CO₂ conversion of 71.3% at 140 °C. The effect of reaction pressure on the catalytic activity was also examined at the temperature of 120 °C and the superficial gas velocity of 24 cm s⁻¹ (Figure 4, top right and Table S9, entry 6-9). The productivity of formate tended to increase proportionally with pressure. This is attributed to the

increase in the solubility of gas reactants in the liquid flow increasing the reaction pressure.

For the investigation of the effect of the Et₃N concentration, the Et₃N feed concentration was adjusted by varying the amount of water in the liquid feed flow by fixing the Et₃N flow rate for the superficial gas velocity of 24 cm s⁻¹, 120 °C, and 12 MPa (Figure 4, bottom left and Table S9, entry 10-14). At a feed concentration of 1 M aqueous Et₃N, the formate productivity was 204.9 g_{form} g_{cat}⁻¹ d⁻¹ with 0.40 of AAR and CO₂ conversion of 40.8% at the superficial gas velocity of 24 cm s⁻¹. When the Et₃N concentration was increased, the catalyst showed improved catalytic activity, reaching 326.8 g_{form} g_{cat}⁻¹ d⁻¹ with 0.61 of AAR and CO₂ conversion of 65.1% at superficial gas velocity of 24 cm s⁻¹ for 3 M of Et₃N. However, at the Et₃N concentration of 5 M, an abrupt decrease in the productivity of the formate was confirmed. Clear phase separation was observed in the product solution for the 5 M Et₃N feed. The reaction did not occur in neat conditions without water. This result supports that water is required for the formation of bicarbonate and for the stabilization of formate adduct in the aqueous phase. Et₃N is immiscible with water (Figure S12). However, in the feed system of Et₃N, H₂O and CO₂ constitutes switchable polarity solvents (SPSs) during CO₂ hydrogenation process, the aqueous Et₃N solution became miscible through formation of Et₃NH⁺:HCO₃⁻ in the presence of CO₂ at the Et₃N concentration lower than 3.2 M (eqn. 7)⁶².



Therefore, the maximum productivity at ca 3.0 M can be closely related to the miscibility of Et₃N and water through bicarbonate formation in the presence of CO₂. Further, it was found that the product miscibility is very much dependent on the concentration of formic acid and feed Et₃N concentration by the obtained ternary phase diagram at 28 °C (Figure S12). If the concentration of formic acid is low, the product solution can become immiscible depending on the concentration of water and Et₃N. As a result, a further reaction was performed in the feed of approx. 3.0 M Et₃N, since an AAR above 0.64 is obtained and the solution is miscible.

In terms of energy, the higher water content in feed requires higher energy consumption in the purification step to concentrate the formic acid. Therefore, the molar ratio of Et₃N to CO₂ was adjusted to 1.00, 0.75, and 0.50 in order to check the probability to decrease the amount of water and amine solvent while the productivity was not affected so much.

To examine this phenomenon closely, the reaction was carried out under the optimal conditions of 120 °C, 12 MPa, and 3M Et₃N feed concentration for varied feed flow rates in order to confirm the dependence of catalytic performance on the superficial gas velocity (Figure 4, bottom right and Table S9, entry 15-25). During the reaction, although the use of a powdery catalyst (0.50 g ml⁻¹ of bulk density, 1.09 g ml⁻¹ and 53.8 % of porosity, Figure S3), no pressure drop was observed. This may contribute to small scale of the reaction size (only 1.5 g of catalyst amount was used) and the particle size was enough for the reaction feed to pass thorough under the conducted hydrogenation conditions. Meanwhile, since the molar ratio of H₂ to CO₂ in the gas feed was maintained at 1:1 (stoichiometric molar ratio), there was no enrichment in the feed gas by the recycling of the unreacted gas stream and little purge is to enhance the process yield.

Under the optimal conditions with Et₃N/CO₂ molar ratio of 1.0, the formate productivity increased as the superficial gas velocity decreased, reaching the highest productivity of a 699. g_{form} g_{cat}⁻¹ d⁻¹ with 0.42 of AAR and CO₂ conversion of 44.8% at the superficial gas velocity of 72 cm s⁻¹. As the molar ratio of Et₃N to CO₂ in feed flow decreased to 0.75, AAR in product increased to 0.7 at the superficial gas velocity of 24 cm s⁻¹, reaching a productivity of 283.5 g_{form} g_{cat}⁻¹ d⁻¹ with CO₂ conversion of 56.9%. This means that the high proportion of gas-phase reactants in the reaction caused itself to be dissolved more in the reaction media, thereby improving the mass transfer of the reagents by increasing the CO₂ solubility. As the flow rate increased, the productivity of formate increased as well, and reached 650.8 g_{form} g_{cat}⁻¹ d⁻¹ with an AAR of 0.54 and CO₂ conversion of 43.6% at the superficial gas velocity of 72 cm s⁻¹. Furthermore, as the amine ratio to CO₂ decreased to 0.5, the AAR increased to the maximum of 0.83, attaining chemical equilibrium⁶³ at the superficial gas velocity of 24 cm s⁻¹, affording 239.0 g_{form} g_{cat}⁻¹ d⁻¹ with CO₂ conversion of 48.0%. With subsequent increase in the flow rate, the productivity reached a 549.4 g_{form} g_{cat}⁻¹ d⁻¹ with an AAR of 0.68 and CO₂ conversion of 36.8% at the superficial gas velocity of 72 cm s⁻¹. Based on the results, the formate productivity

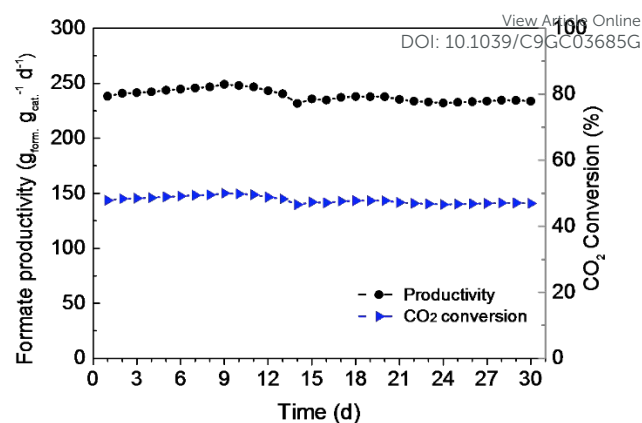


Figure 5. Long-term stability test of the Ru/bpyTN-30-CTF for CO₂ hydrogenation in trickle-bed reactor

and CO₂ conversion decreased as the feed molar ratio of Et₃N to CO₂ decreased; however, the AAR increased.

In order to test the stability of the catalyst in the continuous process, the hydrogenation was carried out under the optimal conditions of 120 °C, 12 MPa, and 3M Et₃N feed concentration with a superficial gas velocity of 24 cm s⁻¹ (Figure 5, bottom right and Table S9, entry 26-54). The reaction products were collected once every 24 hours. As a result, the catalyst exhibited excellent stability for continuous CO₂ hydrogenation process reaching the total turnover number of 524,000 during 30-day operation with only less than 5 % decrease of catalytic performance; a slight drop in catalytic performance was observed on 13th-day stability test, because the reactant feed supply might not stable for a short time. In order to understand the leaching of Ru metal, the liquid phase products collected for 24 h were measured by ICP-OES, showing that the amount of Ru in the products was less than the detection limit (<0.5 ppm). Meanwhile, 2.67 wt% of Ru content in the spent catalyst after the 30-day process was confirmed, which is equal to 0.0005 wt%/h of Ru leaching from the catalyst. This is attributed to the stable coordination of the Ru atoms with the stable binding provided by the abundant N-based sites on the catalyst support derived from bipyridine or triazine groups.

After the reaction, additional measurements were carried out to precisely understand the state of the spent catalyst. STEM and EDS analysis found that no metal particles were present in the spent catalyst after the 30-day reaction and the active metal components were still uniformly distributed throughout the support (Figure 6, top left and middle). Through further EDS analysis, the amount of Cl was confirmed to have decreased due to possible substitution by water and hydride during the reaction, as it is known that Cl does not play a substantial role in hydrogenation (Figure S11).

Then, FT-IR and N₂ isotherm adsorption analysis was conducted to observe the changes in the physical and chemical catalyst structure (Figure 6, top right and bottom left). The catalyst showed almost the same trend of IR spectrum ranges and porosity as the fresh catalyst, suggesting that the catalytic support structure was not decomposed or degraded by the

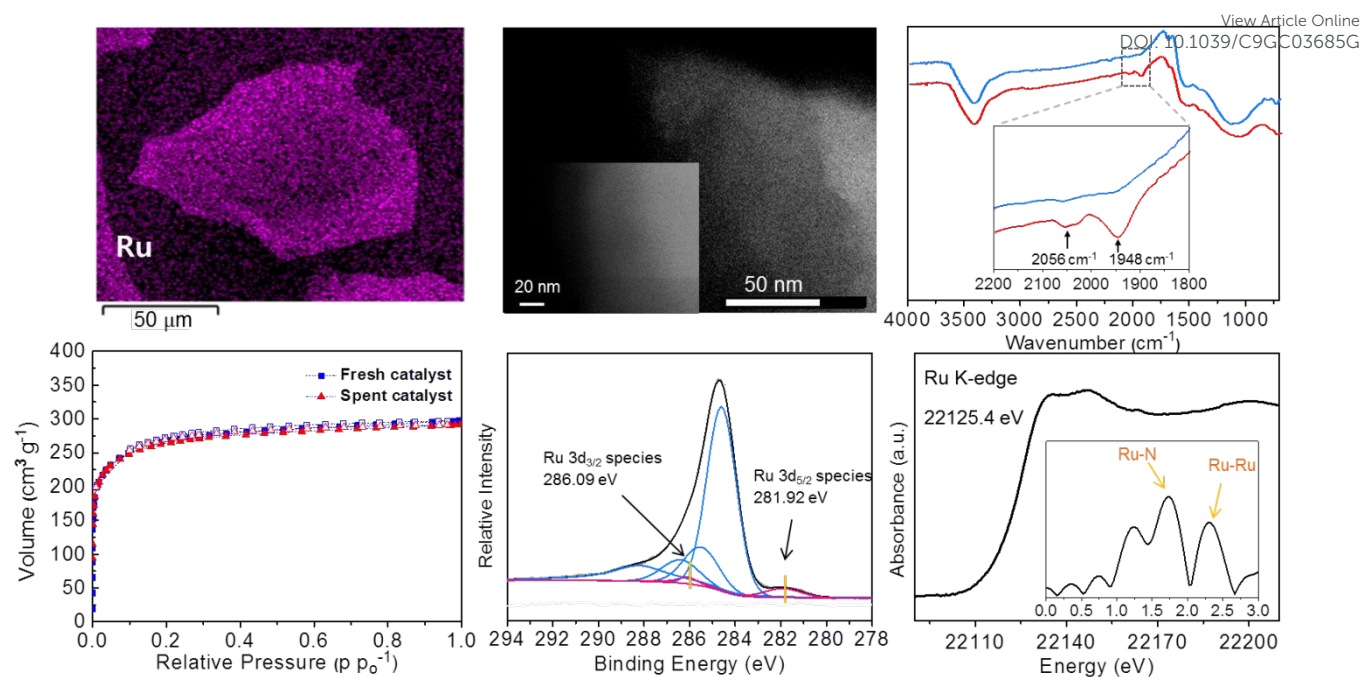


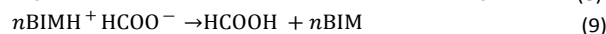
Figure 6. Characterization of the spent Ru/bpyTN-30-CTF. Atomic dispersion of Ru by EDS mapping (top left), HAADF-STEM image (top middle), FT-IR spectra (top right, blue line for fresh catalyst and red line for spent catalyst), N₂ sorption isotherm analysis (bottom left), the normalized XANES spectra at the Ru K-edge (bottom middle), and the k³-weighted EXAFS data in R space (bottom right)

harsh conditions of the CO₂ hydrogenation. In particular, new peaks emerged at 1948 and 2056 cm⁻¹, indicating carbonyl and hydride, respectively, which were generated during the hydrogenation process⁶⁴. The consequence of the oxidation state change of Ru and the ligand exchange effects were analyzed by XPS measurements (Figure 6, bottom middle). The binding energy of Ru in the spent catalyst was 281.92 eV, which indicates that Ru still retained the 3+ oxidation state. Further, this Ru binding energy decreased by 0.09 eV from 282.01 eV for the fresh catalyst, which means that the substituted ligands had a greater electron donation effect than the electronegative chloride. Consistent with this XPS analysis, the Ru K-edge of the spent catalyst was slightly lower in energy than that of the fresh catalyst due to the ligand exchange under the hydrogenation (Figure 6, bottom right). In the EXAFS spectrum, the Ru-Cl peak on 1.9 Å diminished while peaks from Ru-N on ~1.7 Å remained, indicating the substitution of Cl into the other ligands and intact coordination of Ru and N sites from the support; this result was consistent with XPS data.

Validation of formic acid process by CO₂ hydrogenation through the trickle-bed reactor

Here, we propose the feasible process scheme to produce formic acid from CO₂ hydrogenation here. Fresh feed of CO₂ and hydrogen is introduced into the formic acid formation reactor with the recycled gases and the recycled water and Et₃N. The liquid product from the reactor is feeding to the evaporator to concentrate Et₃NH⁺:HCOO⁻ from ~0.83 AAR to ~2.3 AAR. Then, the concentrated Et₃NH⁺:HCOO⁻ adduct with ~2.3 AAR is combined with *n*-butyl imidazole (*n*BIM) and formate adduct (*n*BIMH⁺:HCOO⁻), (0.18 AAR) which is introduced into amine exchange column. In amine exchange

column, the *n*BIMH⁺:HCOO⁻ with 1.0 AAR is produced from the reboiler (eqn. 8), while all the Et₃N is produced in the overhead of the amine exchange column. The *n*BIMH⁺:HCOO⁻ is introduced into formic acid separation column to produce pure formic acid (eqn. 9). A more details are described as follows.



From CO₂ hydrogenation, the Et₃NH⁺:HCOO⁻ adduct is produced in molar ratios of 0.8 with a CO₂ conversion of 48% at 120 °C, 12 MPa, feed Et₃N concentration of 3.0 M, feed molar ratio of Et₃N to CO₂ of 0.5, and superficial gas velocity of 24 cm s⁻¹. Formic acid can be associated to Et₃N with a maximum AAR molar ratio of 2.5⁶⁵. The pKa of Et₃N is 10.8. Due to the strong binding of Et₃N and H⁺ in the cation of Et₃NH⁺, direct separation of formic acid from the adduct of Et₃NH⁺:HCOO⁻ is not achievable. Therefore, the separation process was conducted with reference to a patent claimed by BP chemicals to produce formic acid from the Et₃NH⁺:HCOO⁻: (1) enrichment of formic acid by removing water and Et₃N from the reaction product, (2) amine exchange from Et₃NH⁺:HCOO⁻ to *n*BIM using *n*BIMH⁺:HCOO⁻. Then, (3) formic acid can be produced from the *n*BIMH⁺:HCOO⁻ by a distillation⁶⁶. The enrichment of formic acid from 0.8 of AAR to 2.3 of AAR could be achieved by evaporation using a silver-coated packed glass column (column I.D.: 1 inch, column length: 120 cm, packing material: 1 cm

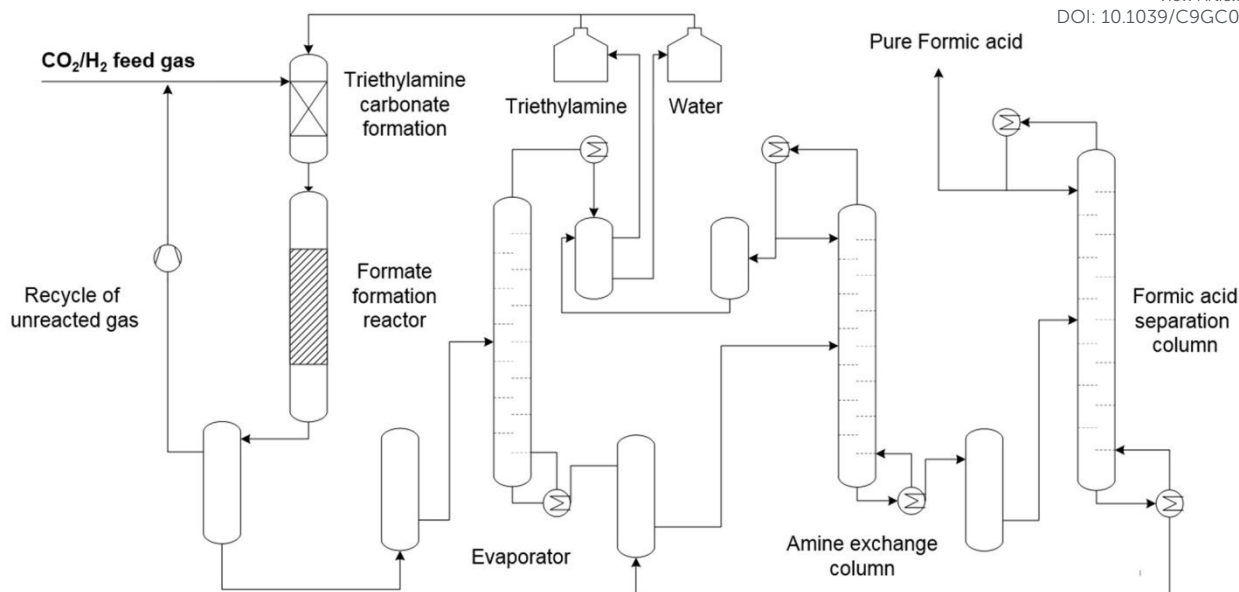


Figure 7. Schematic representation of an integrated TRB reactor system for continuous CO₂ hydrogenation to produce pure formic acid

rash ring) without the recycling of the top product. The operating pressure was 150 mmHg. The feed flow rate (Et₃N: 2.29 g/min, H₂O: 4.38 g/min, formic acid: 0.83 g/min) was 7.5 g/min, which was introduced into the evaporating column through a preheater (100 °C). Due to the low condensing capacity of a lab-scale overhead glass, the overhead temperature was subcooled to 5 °C and a cold trap (−15 °C) was placed before the vacuum pump. No decomposition products were observed by NMR analysis. The reboiler temperature was 140 °C at the steady state and the bottom product flow rate was 1.5–1.6 g/min (AAR was approx. 2.3). An immiscible mixture of water and Et₃N was obtained in the overhead of the evaporator. The experimental results of Et₃N-formic acid were corresponding to earlier reported vapor-liquid equilibrium (VLE)⁶⁵. The azeotropic concentration was reported at the AAR of approx. 2.7. The experimental AAR was less than the azeotropic composition of Et₃N and formic acid. The Et₃NH⁺:HCOO⁻ adduct with the AAR of approx. 2.3 needed to be converted to *n*BIMH⁺:HCOO⁻. The pK_a of *n*BIM (6.9) and the high boiling point of *n*BIM (244.8 °C) can make the amine exchange possible. For the distillation, the same column with random metal packing (5 mm) was used. The feed flow rate (Et₃N: 0.89 g/min, formic acid : 0.94 g/min, *n*BIM: 2.66 g/min) was 4.5 g/min, which was introduced through the preheater (100 °C). The pressure was maintained at 100 mmHg and the overhead condenser temperature and cold trap were maintained at 5 °C and −10 °C, respectively. The reboiler temperature was maintained at 155 °C at the steady state. Only Et₃N was obtained in the overhead and *n*BIMH⁺:HCOO⁻ adduct was obtained. There were no *n*BIM and formic acid in the overhead product. Therefore, it can be concluded that the amine exchange of the second step is valid. Finally, formic acid could be separated from the *n*BIMH⁺:HCOO⁻ adduct. For the distillation, the column length

was 160 cm and the metal random packing was used. The feed flow rate (formic acid: 1.08 g/min, *n*BIM: 2.92 g/min) was 4.0 g/min, which was introduced through the preheater (100 °C). The pressure was maintained at 50 mmHg and the temperatures of the overhead condenser and the cold trap were maintained at 5 °C and −10 °C, respectively. The reboiler temperature was maintained at 145 °C at the steady state. 96 mol% formic acid (1 g/min) was obtained from the overhead product and the molar ratio of formic acid to *n*BIM in the bottom product was 0.17 (15 mol formic acid %). To clarify whether pure formic acid could be separated or not, VLE of *n*BIM and formic acid is necessary. The vapor-liquid equilibrium was obtained (Figure S13) using iFisher VLE apparatus. Based on the VLE data, pure formic acid can be produced from the distillation and it was observed that there was an azeotropic point at approx. 15 mol% formic acid. The simulation of Pro-II for the VLE data gives 21 of theoretical numbers of plates for 99.99% formic acid using NTRL and HOCV model.

Based on the above experiments, it can be concluded that the separation scheme to produce formic acid from Et₃NH⁺:HCOO⁻ adduct is valid. Based on the experimental results, the process to produce formic acid by CO₂ hydrogenation is proposed here as shown in Figure 7.

Conclusions

In summary, heterogenization of a Ru molecular catalyst on a bpyTN-30-CTF support synthesized by the mixed-linker strategy was successfully conducted. The improved porosity and the presence of well-defined binding sites for the metal centers derived from the cooperative network structure of bpy and TN led to both efficient dispersion of active metal sites on

the pore surface and increased electron donation ability to the metal center, resulting in improved catalytic CO₂ hydrogenation activity. Moreover, the heterogeneous character of the Ru/bpyTN-30-CTF allowed it to be suitably exploited in the trickle-bed reactor system, which is a representative fixed-bed reactor for multiphase reactions. In the continuous CO₂ hydrogenation process, the Ru/bpyTN-30-CTF catalyst displayed significant catalytic performance with a highest productivity of 669.0 g_{form.} g_{cat.}⁻¹ h⁻¹ and CO₂ conversion of 44.4 % for a superficial gas velocity of 72 cm s⁻¹. Moreover, superior long-term stability of the Ru/bpyTN-30-CTF catalyst for 30 days reaching the total turnover number of 524,000 without noticeable deactivation demonstrated high feasibility for industrial operation. Based on the results, a new process has been proposed to produce formic acid by CO₂ hydrogenation with an integrated pilot-scale system for the production of pure formic acid with a separation units for the formate adduct, which could lead to a platform for an industrially viable CO₂ hydrogenation process.

Conflicts of interest

There are no conflicts to declare.

Acknowledgements

This work was financially supported by the Korea CCS R&D Center of the Ministry of Science, ICT & Future Planning (2014M1A8A1049300) and the Korea Institute of Science and Technology (KIST). We thanks for professor Jung-Ho Cho in Kongju National University for the discussion on VLE of n-butyl imidazole and formic acid.

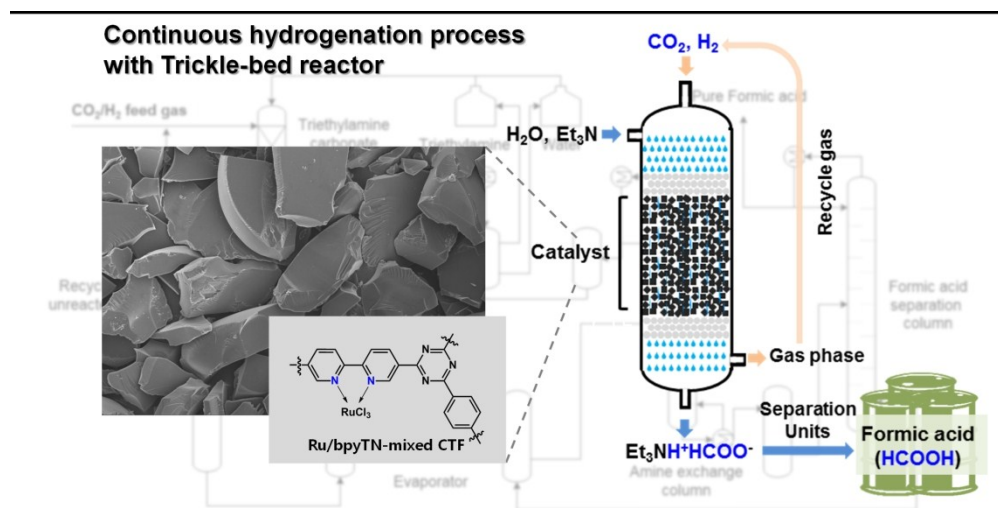
Footnotes

Electronic supplementary information (ESI) available. See DOI:

References

- S. E. Hosseini and M. A. Wahid, *Renew. Sustain. Energy Rev.*, 2016, **57**, 850-866.
- M. R. Shaner, H. A. Atwater, N. S. Lewis and E. W. McFarland, *Energy Environ. Sci.*, 2016, **9**, 2354-2371.
- P. Häussinger, R. Lohmüller and A. M. Watson, *Ullmann's Encyclopedia of Industrial Chemistry*, 2011.
- P. Preuster, C. Papp and P. Wasserscheid, *Acc. Chem. Res.*, 2016, **50**, 74-85.
- D. Teichmann, W. Arlt, P. Wasserscheid and R. Freymann, *Energy Environ. Sci.*, 2011, **4**, 2767-2773.
- S. Enthaler, J. von Langermann and T. Schmidt, *Energy Environ. Sci.*, 2010, **3**, 1207-1217.
- M. Grasmann and G. Laurenczy, *Energy Environ. Sci.*, 2012, **5**, 8171-8181.
- Y. Yang and J.-W. Lee, *Chem. Sci.*, 2019, **10**, 3905-3926.
- M. Peters, B. Koehler, W. Kuckshinrichs, W. Leitner, P. Markewitz and T. E. Müller, *ChemSusChem*, 2011, **4**, 1216-1240.
- M. Aresta, A. Dibenedetto and A. Angelini, *Chem. Rev.*, 2013, **114**, 1709-1742. View Article Online
DOI: 10.1039/C9GC03685G
- Q. Liu, L. Wu, R. Jackstell and M. Beller, *Nat. Commun.*, 2015, **6**, 5933.
- A. Boddien, C. Federsel, P. Sponholz, D. Mellmann, R. Jackstell, H. Junge, G. Laurenczy and M. Beller, *Energy Environ. Sci.*, 2012, **5**, 8907-8911.
- T. C. Johnson, D. J. Morris and M. Wills, *Chem. Soc. Rev.*, 2010, **39**, 81-88.
- D. Mellmann, P. Sponholz, H. Junge and M. Beller, *Chem. Soc. Rev.*, 2016, **45**, 3954-3988.
- B. Loges, A. Boddien, F. Gärtner, H. Junge and M. Beller, *Top. Catal.*, 2010, **53**, 902-914.
- K. Sordakis, C. Tang, L. K. Vogt, H. Junge, P. J. Dyson, M. Beller and G. Laurenczy, *Chem. Rev.*, 2017, **118**, 372-433.
- GRT group (2019), Hyform-PEMFC; <https://grtgroup.swiss/> (accessed 19 July 2019).
- R. van Putten, T. Wissink, T. Swinkels and E. A. Pidko, *Int. J. Hydrogen Energy*, 2019. doi:10.1016/j.ijhydene.2019.01.153
- W. Leitner, *Angew. Chem. Int. Ed. Engl.*, 1995, **34**, 2207-2221.
- P. G. Jessop, T. Ikariya and R. Noyori, *Chem. Rev.*, 1995, **95**, 259-272.
- W. Wang, S. Wang, X. Ma and J. Gong, *Chem. Soc. Rev.*, 2011, **40**, 3703-3727.
- A. Behr and K. Nowakowski, in *Adv. Inorg. Chem.*, Elsevier, 2014, vol. 66, pp. 223-258.
- L. Wu, Q. Liu, R. Jackstell and M. Beller, in *Carbon Dioxide and Organometallics*, Springer, 2015, pp. 279-304.
- W.-H. Wang, Y. Himeda, J. T. Muckerman, G. F. Manbeck and E. Fujita, *Chem. Rev.*, 2015, **115**, 12936-12973.
- T. Schaub and R. A. Paciello, *Angew. Chem. Int. Ed.*, 2011, **50**, 7278-7282.
- T. Schaub, R. A. Paciello, K. D. Mohl, D. Schneider, M. Schäfer and S. Rittinger, WO2010149507A2, 2010.
- T. Schaub, O. Bey, A. Meier, D. Fries and R. Hugo, WO2013050367A2, 2013.
- We take care of equipment systems amp space to let you focus on whats important converting carbon dioxide. <http://www.carboncenter.org/> (accessed 19 July, 2017).
- Pilot & Test Center|ReactWell. <http://www.reactwell.com/case-studies/test-center/> (accessed 19 July, 2017).
- W. Leitner, U. Hintermair, S. Wesselbaum, WO Patent 2,012,095,345, 2012.
- M. Scott, B. Blas Molinos, C. Westhues, G. Franciò and W. Leitner, *ChemSusChem*, 2017, **10**, 1085-1093.
- C. M. Jens, M. Scott, B. Liebergesell, C. G. Westhues, P. Schäfer, G. Franciò, K. Leonhard, W. Leitner and A. Bardow, *Adv. Synth. Catal.*, 2019, **361**, 307-316.
- J. Artz, T. E. Müller, K. Thenert, J. Kleinekorte, R. Meys, A. Sternberg, A. Bardow and W. Leitner, *Chem. Rev.*, 2017, **118**, 434-504.
- G. H. Gunasekar, K. Park, K.-D. Jung and S. Yoon, *Inorg. Chem. Front.*, 2016, **3**, 882-895.
- A. Álvarez, A. Bansode, A. Urakawa, A. V. Bavykina, T. A. Wezendonk, M. Makkee, J. Gascon and F. Kapteijn, *Chem. Rev.*, 2017, **117**, 9804-9838.
- D. A. Bulushev and J. R. Ross, *Catal. Rev.*, 2018, **60**, 566-593.
- W.-H. Wang, X. Feng and M. Bao, in *Transformation of Carbon Dioxide to Formic Acid and Methanol*, Springer, 2018, pp. 43-52.
- D. Preti, C. Resta, S. Squarcialupi and G. Fachinetti, *Angew. Chem. Int. Ed.*, 2011, **50**, 12551-12554.
- S. Wesselbaum, U. Hintermair and W. Leitner, *Angew. Chem. Int. Ed.*, 2012, **51**, 8585-8588.
- K. Park, G. H. Gunasekar, N. Prakash, K. D. Jung and S. Yoon, *ChemSusChem*, 2015, **8**, 3410-3413.

- 41 G. H. Gunasekar, J. Shin, K.-D. Jung, K. Park and S. Yoon, *ACS Catalysis*, 2018, **8**, 4346-4353.
- 42 G. H. Gunasekar, K.-D. Jung and S. Yoon, *Inorg. Chem.*, 2019, **58**, 3717-3723
- 43 J. J. Corral-Pérez, A. Billings, D. Stoian and A. Urakawa, *ChemCatChem*, 2019, **11**, 4725-4730
- 44 V. V. Ranade, R. Chaudhari and P. R. Gunjal, *Trickle bed reactors: Reactor engineering and applications*, Elsevier, **2011**.
- 45 L.-Y. Liao, X.-R. Kong and X.-F. Duan, *J. Org. Chem.*, 2014, **79**, 777-782.
- 46 P. Kuhn, M. Antonietti and A. Thomas, *Angew. Chem. Int. Ed.*, 2008, **47**, 3450-3453.
- 47 M. Liu, L. Guo, S. Jin and B. Tan, *J. Mater. Chem. A*, 2019, **7**, 5153-5172.
- 48 J. Artz, *ChemCatChem*, 2018, **10**, 1753-1771.
- 49 G. H. Gunasekar, K. Park, V. Ganesan, K. Lee, N.-K. Kim, K.-D. Jung and S. Yoon, *Chem. Mater.*, 2017, **29**, 6740-6748.
- 50 G. Gunasekar, K. Park, H. Jeong, K.-D. Jung, K. Park and S. Yoon, *Catalysts*, 2018, **8**, 295.
- 51 A. V. Bavykina, E. Rozhko, M. G. Goesten, T. Wezendonk, B. Seoane, F. Kapteijn, M. Makkee and J. Gascon, *ChemCatChem*, 2016, **8**, 2217-2221.
- 52 S. Dey, A. Bhunia, H. Breitzke, P. B. Groszewicz, G. Buntkowsky and C. Janiak, *J. Mater. Chem. A*, 2017, **5**, 3609-3620.
- 53 S. Dey, A. Bhunia, I. Boldog and C. Janiak, *Microporous Mesoporous Mater.*, 2017, **241**, 303-315. View Article Online
DOI: 10.1039/C9GC03685G
- 54 A. Bhunia, I. Boldog, A. Möller and C. Janiak, *J. Mater. Chem. A*, 2013, **1**, 14990-14999.
- 55 S. Hug, M. B. Mesch, H. Oh, N. Popp, M. Hirscher, J. Senker and B. V. Lotsch, *J. Mater. Chem. A*, 2014, **2**, 5928-5936.
- 56 K. Park, K. Lee, H. Kim, V. Ganesan, K. Cho, S. K. Jeong and S. Yoon, *J. Mater. Chem. A*, 2017, **5**, 8576-8582.
- 57 S. Hug, L. Stegbauer, H. Oh, M. Hirscher and B. V. Lotsch, *Chem. Mater.*, 2015, **27**, 8001-8010.
- 58 F. Wang, Q. Xu, Z. a. Tan, L. Li, S. Li, X. Hou, G. Sun, X. Tu, J. Hou and Y. Li, *J. Mater. Chem. A*, 2014, **2**, 1318-1324.
- 59 D. J. Morgan, *Surf. Interface Anal.*, 2015, **47**, 1072-1079.
- 60 K. Mori, T. Taga and H. Yamashita, *ACS Catalysis*, 2017, **7**, 3147-3151.
- 61 S. Yamaguchi, K. Kamiya, K. Hashimoto and S. Nakanishi, *Chem. Commun.*, 2017, **53**, 10437-10440.
- 62 P. G. Jessop, S. M. Mercer and D. J. Heldebrant, *Energy Environ. Sci.*, 2012, **5**, 7240-7253.
- 63 Y. Himeda, *Eur. J. Inorg. Chem.*, 2007, **2007**, 3927-3941.
- 64 A. Kann, H. Hartmann, A. Besmehn, P. J. Hausoul and R. Palkovits, *ChemSusChem*, 2018, **11**, 1857-1865.
- 65 K. Narita and M. Sekiya, *Chem. Pharm. Bull.*, 1977, **25**, 135-140.
- 66 J. J. Anderson, D. J. Drury, J. E. Hamlin and A. G. Kent (BP), US4855496A, 1989.



369x186mm (150 x 150 DPI)